



Climate-driven variations in suspended particulate matter dominate water clarity in shallow lakes

CHONG FANG,^{1,2} PIERRE-ANDRE JACINTHE,³ CHANGCHUN SONG,^{1,2} CHI ZHANG,¹ AND KAISHAN SONG^{2,4,*}

¹Faculty of infrastructure engineering, Dalian University of Technology, Dalian 116024, China

²Northeast Institute of Geography and Agroecology, Chinese Academy of Sciences, Changchun 130102, China

³Department of Earth Sciences, Indiana University-Purdue University Indianapolis, IN, USA

⁴School of Environment and Planning, Liaocheng University, Liaocheng 252000, China

*songkaishan@iga.ac.cn

Abstract: Secchi disk depth (SDD) has long been considered as a reliable proxy for lake clarity, and an important indicator of the aquatic ecosystems. Meteorological and anthropogenic factors can affect SDD, but the mechanism of these effects and the potential control of climate change are poorly understood. Preliminary research at Lake Khanka (international shallow lake on the China-Russia border) had led to the hypothesis that climatic factors, through their impact on suspended particulate matter (SPM) concentration, are key drivers of SDD variability. To verify the hypothesis, Landsat and MODIS images were used to examine temporal trend in these parameters. For that analysis, the novel SPM index (SPMI) was developed, through incorporation of SPM concentration effect on spectral radiance, and was satisfactorily applied to both Landsat ($R^2 = 0.70$, $p < 0.001$) and MODIS ($R^2 = 0.78$, $p < 0.001$) images to obtain remote estimates of SPM concentration. Further, the SPMI algorithm was successfully applied to the shallow lakes Hulun, Chao and Hongze, demonstrating its portability. Through analysis of the temporal trend (1984–2019) in SDD and SPM, this study demonstrated that variation in SPM concentration was the dominant driver (explaining 63% of the variation as opposed to 2% due to solar radiation) of SDD in Lake Khanka, thus supporting the study hypothesis. Furthermore, we speculated that variation in wind speed, probably impacted by difference in temperature between lake surface and surrounding landscapes (greater difference between 1984–2009 than after 2010), may have caused varying degree of sediment resuspension, ultimately controlling SPM and SDD variation in Lake Khanka.

© 2022 Optica Publishing Group under the terms of the [Optica Open Access Publishing Agreement](#)

1. Introduction

Lakes are important components of the biosphere, contributing to atmospheric processes and regulation of regional climate through primary production, carbon storage and greenhouse gases emission. Lakes also play economical functions and have been exploited as sources of water for agriculture, aquaculture, recreation and drinking water [1–4]. In addition, several large lakes serve as borders between neighboring countries (eg. the Great Lakes, Lake Khanka), and thus are of international and political significance [5].

Secchi disk depth (SDD) is the depth of light penetration in a lacustrine system, and has traditionally been measured by lowering a disk (black-white or white) into the water column, the depth of just right invisible for an observer at the surface [6,7]. SDD has long been used to express lake water clarity, and has been adopted as a reliable proxy for lake water quality evaluation [6,8–10]. SDD has been linked to the three major optically-active components (OAC) in natural waters, including suspended particulate matter (SPM), chlorophyll a (Chla) and dissolved organic

carbon (DOC) [3,7,11]. SDD substantially affects the underwater light environment in aquatic ecosystems and is a significant index of lake trophic status [12–14]. Due to its convenient operation and relatively cheapness, SDD has widely been used as a surrogate of water quality and guide lacustrine ecosystem maintenance efforts [9,13,15]. However, for large water bodies, continuous monitoring of SDD still poses logistical challenges.

Given the opportunity for large-scale synchronous observations and the availability of long-term dataset, satellite images have become a mainstream data source to research global and regional aquatic environments [3,7,11]. This is especially relevant to the monitoring of water quality in the world's large lakes. Several sensors have been used for that purpose, and include MultiSpectral Imager (MSI), Ocean and Land Colour Instrument (OLCI), Moderate Resolution Imaging Spectroradiometer (MODIS) and Landsat series of sensors. Compared to other sensors, MODIS and Landsat TM/ETM+/OLI (TM: 1984–2012; ETM+: 1999–Now; OLI: 2013–Now) often provide the optimal combination of frequent revisit (MODIS has daily reflectance dataset from 2000) and long-term coverage (Landsat has the longest data acquisition history, since the 1970's) [16]. Numerous SDD models have been constructed to calculate lacustrine SDD, including empirical [17–21], Forel-Ule Index [7] and semi-analytical algorithms [22–24]. Empirical models are most widely used due to their simplicity and computational efficiency.

Recently, the long-term variation in SDD and related driving forces have been studied, and the trends of SDD have been examined in order to identify underlying driving factors and propose effective management measures [2,7,10,12]. [7] found that increase in lake SDD was strongly correlated with changes in economic development, surrounding environment factors and water area. [2] noted that lake expansion was a key factor for the observed increase in SDD in alpine lakes of the Tibetan Plateau. [11] demonstrated that human activities had a greater influence than natural forces on SDD in the large lakes of the Yangtze Plain. [25] documented the effects of precipitation on the long-term variation of SDD. It should be noted the studies reviewed above have largely been regional and country-wide in scope and, although several relevant factors of SDD variability have been identified, the underlying mechanisms of these controls remain poorly understood.

Meteorological and anthropogenic factors can either directly or indirectly affect lake SDD through increased concentration of SPM and other OAC [12]. Past researches have demonstrated that climatic factors including temperature (TEMP), precipitation (PRCP), wind speed (WDSP), atmospheric pressure (AP), and solar radiation (which is highly related to sunshine hours, SH) can have major influences on lacustrine sustainability [12,26,27]. Furthermore, these factors can significantly enhance or weaken the influence of anthropogenic activities on lacustrine ecology. For example, mining could affect SDD through increased SPM and Chla [28,29], but these impacts can be further amplified by increased rainfall through greater delivery of nutrients and sediment-laden runoff from surrounding drainage basins [30,31]. Therefore, identifying drivers of interannual variability in lake SDD can be challenging in some contexts. To unravel this question, our research group has monitored the hydro-chemical conditions of Lake Khanka, a large shallow lake between China and Russia, and recorded substantial variations in SPM and SDD for several years. Consistently low concentrations of both Chla and DOC were recorded in Lake Khanka. With the knowledge that the lake's bottom sediments are dominated by clay [32] and there is limited disturbing anthropogenic activities (e.g. mining, sand dredging) in the drainage basin, observed variation in SPM and SDD was assumed to be predominantly controlled by climatic factors but that has not been verified. It remains also unclear whether the influence of these climatic factors may have varied during the last several decades in response to changing local climate.

In order to verify the above hypothesis and elucidate linkages between climate change and SDD variability in lakes, this study was designed with three objectives: (1) developing robust models for SDD and SPM using in-situ data and satellite (Landsat and MODIS) images, (2)

mapping the spatiotemporal variation of SDD and SPM in Lake Khanka between 1984–2019 and investigating temporal trends in these water quality metrics, and (3) quantifying the relative contribution of identified driving forces and clarifying how climate change may have affected SDD during the observation period.

2. Materials and methods

2.1. Acquisition and analysis of field data

Lake Khanka is China's largest international boundary lake, and is located at the junction of China and Russia ($131.97^{\circ}\sim 132.86^{\circ}\text{E}$, $44.51^{\circ}\sim 45.41^{\circ}\text{N}$, Fig. 1). An elongated hill cuts across the lake, dividing Lake Khanka into Great Khanka and Small Khanka. Small Khanka is a typical shallow lake (surface water area: 148 km^2 ; mean depth: 1.8 m). Great Khanka covers a total area of $4,139\text{ km}^2$ ($1,193\text{ km}^2$ in China, $2,946\text{ km}^2$ in Russia), which is a typical shallow lake (average depth: 3.5 m). Lake Khanka is located in the northern temperate monsoon climate zone. Due to its high latitude location, Lake Khanka experiences long periods of freezing, from early November to the end of April.

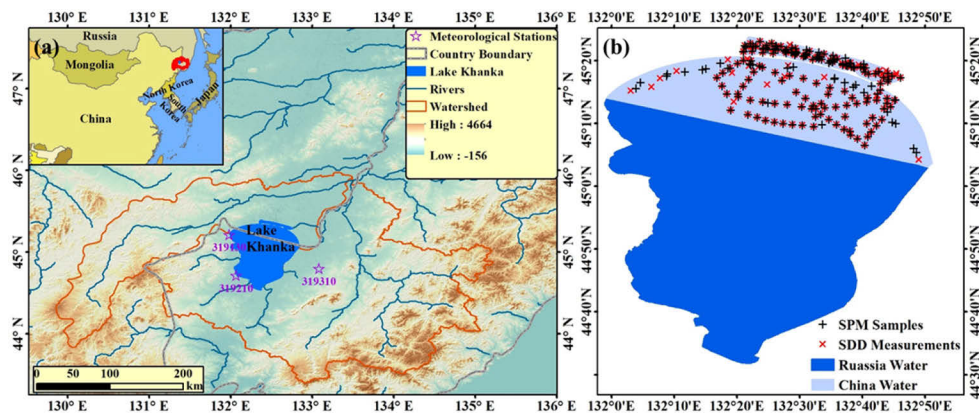


Fig. 1. Lake Khanka and surrounding drainage basin. (a) location, topography, watershed boundary, and meteorological stations near Lake Khanka; (b) location of the sampling sites where secchi disk depth (SDD) was measured and water samples were collected for measurement of suspended particulate matter (SPM).

Field data was collected in Lake Khanka between May and October each year, from 2012 to 2018. Sampling stations were distributed across Small Khanka and in the Chinese section of Great Khanka (Fig. 1). Samples obtained in field were stored in black acid-washed plastic bottles (1-L), transported on ice, and stored at 4°C in a refrigerator. Water samples were analyzed within 2 days in laboratory. Concentration of SPM in field acquired samples was carried out weight analysis in the laboratory using pre weighted $0.7\text{ }\mu\text{m}$ glass microfibre filters (Whatman, GF/F 1825-047) [33]. Chla was extracted from water samples with 90% buffered acetone solution, and its concentration was measured spectrophotometrically using a Shimadzu UV-2660 PC spectrophotometer [34]. DOC was measured using filtered water samples through $0.45\text{ }\mu\text{m}$ mixing fiber Millipore filters. The value was difference of the dissolved inorganic carbon and the dissolved total carbon, both of them were measured through high-temperature catalytic oxidation (680°C) using a Shimadzu Total Organic Carbon Analyzer (TOC-VCPN, Shimadzu Corporation, Japan) [35,36].

2.2. Satellite images processing

2.2.1. Satellite images acquisition

A bulk of Landsat Surface Reflectance Product covering Lake Khanka, and non-snow-covered months during 1984–2019 were obtained from the Google Earth Engine (GEE) (<https://code.earthengine.google.com/>). This dataset is the atmospherically corrected surface reflectance through LEDAPS and LaSRC algorithm by USGS [37–39]. The cloud of all images was masked via setting the attributes of pixel_qa on cloud and shadow in GEE platform before downloading [40]. The gap problem in ETM+ images could be resolved through the ‘DEM_BAD_DATA_DOIT’ function, and calculating the mean reflectance of adjacent pixels to repair the defective pixels [41,42]. The downloaded images contained 5 bands, blue, green, red, near-infrared (NIR) and short wave infrared (SWIR) bands.

The MODIS images are composed of MOD09GA and MYD09GA data, which are daily surface reflectance products of Terra and Aqua, respectively. We downloaded every May to October images from 2000 to 2019 from NASA’s Land Processes Distributed Active Archive Center (LP-DAAC) (<https://ladsweb.modaps.eosdis.nasa.gov/search/>). After reprojection to Albers from sinusoidal projection, band 1~5 were combined and Quality Control (QC) were reserved to remove bad and cloud-contaminated pixels. Further processing details can be found in [16]. The blue, green, red, NIR and SWIR bands were arranged in order from 1 to 5 in the processed images. The value from MODIS and Landsat images was surface reflectance (SR) after atmospheric correction, and remote sensing reflectance (Rrs) was computed by dividing π from SR.

2.2.2. Water region mask and images filtering

The Modified Normalized Difference Water Index (MNDWI) was selected to determine the surface water boundary of Lake Khanka [43], the threshold was determined by an automatic threshold selection method [16]. We chose one cloudless Landsat image from 1984 to 2019 to extract the water body for Lake Khanka, then compared and selected the smallest water boundary in the past 36 years. In order to avoid the interference from mixed pixel of land and water, the selected boundary was buffered inward two pixels as to be the final water region mask of Landsat and MODIS. All downloaded Landsat and MODIS images were batch-clipped by the water mask region through IDL 8.5 software (ESRI Inc. Redlands, CA, USA). Subsequent images processing was based on the above clipped images. When invalid lake area in each image was more than 25% of the selected lake area, this image was not used in further processing to avoid the error caused by incomplete image.

2.3. Statistical analyses

2.3.1. Algorithm assessment

For assessing the performance of the algorithm, the mean relative error (MRE) and root mean square error (RMSE) were conducted as follows:

$$MRE = \frac{1}{N} \times \sum_{i=1}^N \left| \frac{x_i - y_i}{x_i} \right| \times 100\% \quad (1)$$

$$RMSE = \sqrt{\frac{\sum_{i=1}^N \left(\frac{x_i - y_i}{x_i} \right)^2}{N}} \quad (2)$$

where N is the number of validation samples, x_i and y_i refer to the measured value and predicted value.

2.3.2. Relative contribution of factors

In order to explore the relative contribution of each influencing factor on the inter-annual variation of lake SDD, a multiple general linear model (GLM) regression analysis was calculated [11,44]. To reduce the effects of autocorrelation among different variables, the stepwise option of the GLM was implemented. Stepwise option was conducted using the IBM SPSS statistical software package and further GLM were processed using R language.

2.4. Estimation of SDD

Match-ups between SDD measured in-situ and estimate of SDD derived from processed OLI/ETM+ or MOD09GA/MYD09GA images collected were used to develop SDD retrieval models. Since the relatively stable water quality of Lake Khanka, images with time interval of more than 1 day also were used, but most matching points were kept within 24 hours (Table S2). After removing invalid points resulting from land-water boundary, pixels contaminated by cloud shadow, a total of 103 and 128 matched-pairs were reserved for Landsat and MODIS images, respectively. We randomly divided all valid pairs into calibration and validation dataset in a ratio of 2:1. Therefore, 69 and 84 samples were used to calibrate the Landsat and MODIS models, and 34 and 44 samples were applied to the validation of the Landsat and MODIS models, respectively. After testing and comparing several algorithms, we further adjusted the Red/Green ratio model proposed by [20] into a Green/ Red model. Our calibration and validation dataset confirmed the adjusted algorithm was strong and promising (Fig. 2). More details about the model comparison and selection can be found in Section 4.1. The algorithms based on Landsat and MODIS images were as follows:

$$SDD_{Landsat} = 0.1631 \times \exp\left(5.1092 \times \frac{Rrs(Green)}{Rrs(Red)}\right) \quad (3)$$

$$SDD_{MODIS} = 0.4554 \times \exp\left(4.1823 \times \frac{Rrs(555)}{Rrs(645)}\right) \quad (4)$$

The above algorithms performed very well as indicated by the high coefficients of determination (Landsat: $R^2 = 0.83$, $p < 0.001$; MODIS: $R^2 = 0.81$, $p < 0.001$) (Fig. 2). In the calibration datasets of Landsat and MODIS, almost all samples fell within the 95% confidence interval (Fig. 2(a), c). Though the MRE and RMSE of Landsat model was slightly higher than with the MODIS model, in both cases measured and estimated SDD values were evenly distributed along the 1:1 line (Fig. 2(b), d). Thence, these two models were deemed adequate for mapping SDD using Landsat and MODIS images.

2.5. Estimation of SPM

2.5.1. Derivation of SPMI

Various SPM retrieval models have been proposed, ranging from semi-analytical to empirical regression models [45–48]. Although analytical or semi-analytical models may have been more suitable for this lake, it would have been expensive to measure the many parameters required to run these models. In this study, however, a suitable semi-empirical SPM model was built and applied successfully to derive SPM distribution in Lake Khanka from satellite imagery. The success of the SPMI model lies in the recognition that Landsat and MODIS images spectra varied with different concentration of SPM. Typical spectra of Landsat and MODIS images for various concentrations of SPM are presented in Fig. 3.

Three inference rules are typically applied to Landsat and MODIS data (Fig. 3(a)). First, the reflectance of the red band increases with augmentation in SPM concentration for some points (eg. 16 mg/L, 28 mg/L, 54 mg/L, 70.67 mg/L, 93.33 mg/L). Second, when the green band reflectance of two or more samples is very similar, along with the reflectance difference between the red and green bands shrinks, the SPM concentration increases for some points (eg. 16 mg/L and 54

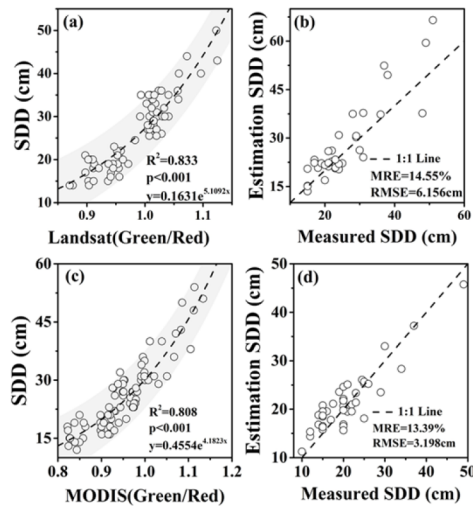


Fig. 2. Algorithms for remote estimation of secchi disk depth (SDD) with Landsat (a) and MODIS (c) images. Assessment of the Landsat (b) and MODIS (d) algorithms through comparison of predicted and measured SDD. Shaded area represents the 95% confidence interval.

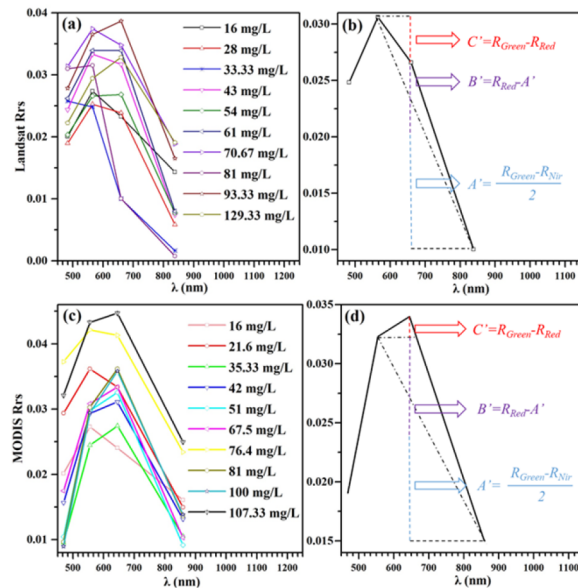


Fig. 3. Typical reflectance spectra of Landsat and MODIS in function of suspended particulate matter (SPM) concentration.

mg/L; 43 mg/L and 61 mg/L; 70.67 mg/L and 93.33 mg/L). Third, when the red band reflectance of two or more samples is very similar, as the reflectance difference between the green and Nir bands shrinks, the SPM concentration increases for some points (eg. 61 mg/L and 70.67 mg/L; 28 mg/L and 129.33 mg/L). In light of these rules, typical spectral curves of both Landsat and MODIS images are summarized and simplified using the schematic diagram in Fig. 3. The typical spectral curves of Landsat and MODIS were demonstrated in Fig. 3(a) and (c), we could derive the average spectral values (Fig. 3(b) and (d)). From the three inference rules of the spectral

variation characteristics under different SPM concentration mentioned above, some relationships were revealed between SPM concentration and Rrs_{Red} , Rrs_{Nir} , the difference between Rrs_{Green} and Rrs_{Nir} , the difference between Rrs_{Green} and Rrs_{Red} . In order to summarize the discovered rules into an algorithm, all of above differences were projected into a same dimension, that's the origin of A', B', C' and SPMI. Since SPMI is an index used to derive SPM concentration, which is greater than 0 in a practical sense, so the absolute value symbol was added in Eq. (5).

Based on the above analysis, the SPMI for estimating the concentration of SPM was constructed as shown in Eq. (5) and Eq. (6).

$$SPMI = \left| \frac{[Rrs_{Red} - 0.5 \times (Rrs_{Green} - Rrs_{Nir})] - (Rrs_{Green} - Rrs_{Red})}{2} \right| \quad (5)$$

$$SPMI = \left| Rrs_{Red} - \frac{3}{4} \times Rrs_{Green} + \frac{1}{4} Rrs_{Nir} \right| \quad (6)$$

2.5.2. SPM algorithm development and validation

Matching point-pairs between SPM measured in-situ and information from the processed OLI/ETM+ or MOD09GA/MYD09GA image collected were used to develop SPM retrieval models. After deleting invalid points caused by land-water boundary, cloud/shadow-contaminated pixels, a total of 105 and 130 matched pairs were reserved for Landsat and MODIS images, respectively. Random 2/3 of the synchronous matching data between field SPM with Landsat images ($N = 79$) and MODIS/Aqua images ($N = 86$) to construct the models. The remaining 1/3 of the samples were used for models validation ($N = 36$ for Landsat; $N = 44$ for MODIS). The calibration and validation dataset confirmed that the SPMI-based model can yield satisfactory results (Fig. 4). Thus, the following algorithms were used for Landsat and MODIS images:

$$SPM_{Landsat} = 8496.29 \times SPMI - 34.159 \quad (7)$$

$$SPM_{MODIS} = 6757.57 \times SPMI - 34.481 \quad (8)$$

The algorithms based on SPMI produced reasonably accurate results as shown by the high determination coefficients (Landsat: $R^2 = 0.70$, $p < 0.001$; MODIS: $R^2 = 0.78$, $p < 0.001$) (Fig. 4).

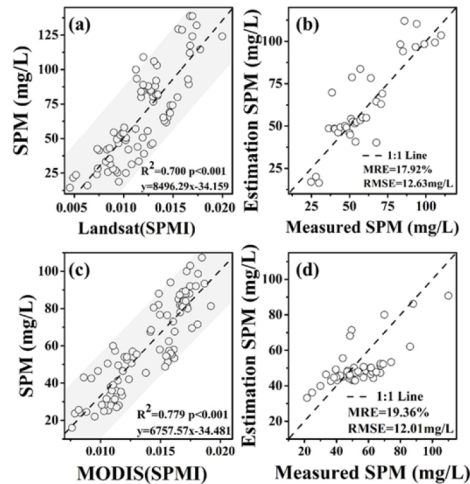


Fig. 4. Algorithms for remote estimation of suspended particulate matter (SPM) with Landsat (a) and MODIS (c) images. Assessment of the Landsat (b) and MODIS (d) algorithms through comparison of predicted and measured SPM. Shaded area represents the 95% confidence interval.

In the calibration dataset, for both Landsat and MODIS, almost all data points fell within the 95% confidence interval (Fig. 4(a), c). Furthermore, the MRE and RMSE values for the Landsat model were extremely close to those of the MODIS model and, for both models, measured and estimated SPM values were evenly distributed along the 1:1 line (Fig. 4(b), d). Thence, the above two models were determined to be consistent and adequate for SPM mapping using Landsat and MODIS images. Additionally, in case of possible negative values resulted by very small SPMI, the negative pixels have been unified set to 0.

2.6. Auxiliary datasets

We assembled two sets of meteorological data. Solar radiation data was obtained from the National Meteorological Information Center (<http://data.cma.cn/>). Other meteorological data, including daily average TEMP, PRCP, WDSP and AP were obtained from the NOAA National Meteorological Information Center (<https://gis.ncdc.noaa.gov/maps/ncei>). Monthly averages of these above meteorological parameters were computed from daily data. The annual average of SH, PRCP, WDSP and AP was the mean of their respective monthly average between May to October each year.

3. Results

3.1. Spatiotemporal variation of SDD and SPM

The retrieval algorithms of SDD and SPM in Eq. (3) and (7) were applied to 198 Landsat scenes collected between 1984 and 2019 (Table S5), from which annual arithmetic mean SDD and SPM products were generated and mapped (Fig. 5 and Fig. 6).

From 1984 to 2019, the SDD in Lake Khanka exhibited distinct spatial and inter-annual distributions (Fig. 5). A significant increasing trend was observed in the past 36 years, from an average of 14 cm in 1984 to 19 cm in 2019. The inter-annual maximum SDD was recorded in 2010, and that was followed by a slowly decreasing trend in SDD. Averaged across the entire Lake Khanka, mean SDD was 18 cm during the period 1984–1999 and 25 cm during the period 2000–2019. Spatial examination of the results also showed that SDD was consistently greater on the lacustrine western side than on the eastern side of the lake (Fig. 5).

Unlike the temporal trend observed with SDD, SPM values across Lake Khanka showed a continuous decreasing trend over the 36 years of observation, from 90.21 mg/L in 1984 to 74.66 mg/L in 2019 (Fig. 6). The inter-annual minimum SPM was also observed in 2010, after which SPM slowly but significantly increased. Across the entire Lake Khanka, mean SPM was higher (63.94 mg/L) during the period 1984–1999 than during the 2000–2019 period (mean: 54.15mg/L). Consistent with the spatial distribution of SDD, there was a clear west–east gradient in SPM, with more turbid waters in the eastern than in the western section of Lake Khanka (Fig. 6).

3.2. Inter-annual variation of SDD and SPM in different lake areas

The temporal trend in SDD and SPM during the observation period (1984 - 2019) was examined in different sections of Lake Khanka (Fig. 7). Using linear regression curve fitting (Fig. 7(a)), the inter-annual change in SDD was similar in the China's and Russia's portion of Khanka Lake. However, these temporal trends were drastically different for Small Khanka. Morphometrically different than the other lacustrine regions, Small Khanka showed a continuous and more rapid increasing trend in SDD (as indicated by the greater slope of the regression; Fig. 7(a)). While variations in SDD remained relatively stable from 1984 to 1999, the amplitude of that variation became much greater since 2000 (Fig. 7(a)).

SPM exhibited almost the opposite temporal trend compared to the variation in SDD that is a progressive decline during the observation period (Fig. 7(b)). Again, great similarity was

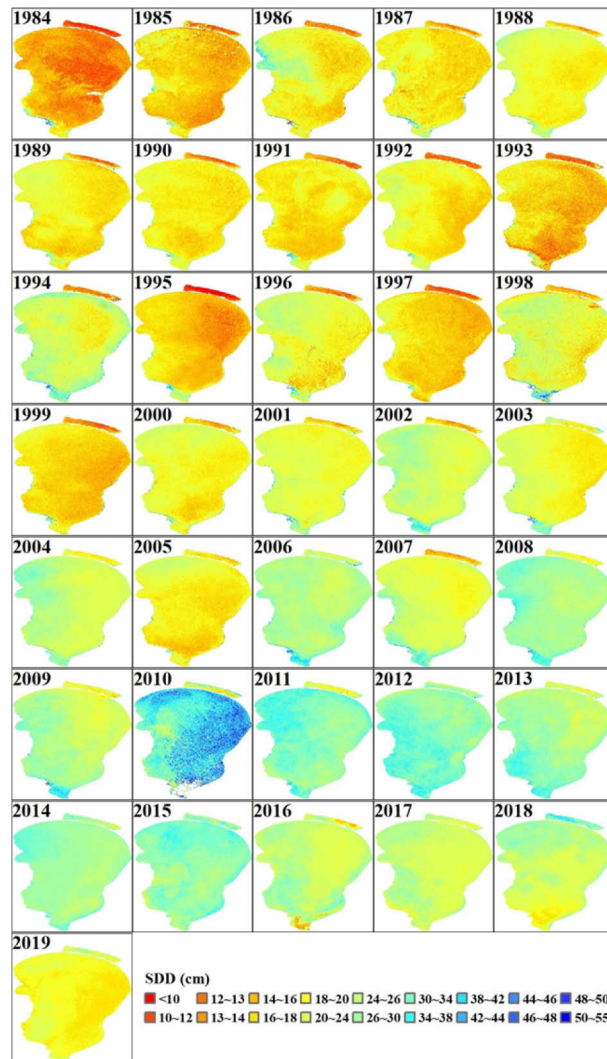


Fig. 5. Spatial distribution of mean annual (1984–2019) secchi disk depth (SDD) across Lake Khanka derived from Landsat images.

observed in terms of the inter-annual variation in SPM in the China's and Russia's portion of Lake Khanka. Specifically, in the much shallower Small Khanka, the decreasing trend in SPM was more rapid (higher slope of the regression; Fig. 7(b)).

3.3. Monthly pattern of SDD and SPM

The estimation models of SDD and SPM, shown in Eq. (4) and (8), were applied to 2,212 scenes of MODIS images from 2000 to 2019 and (Table S6), based on these estimations, average monthly distribution of SDD and SPM in different lacustrine regions of Lake Khanka were calculated (Figure S1).

For the entire Lake Khanka, the average SDD was highest in May (34.84 ± 11.71 cm), lowest in October (21.50 ± 5.39 cm), with limited variation in the other months (Figure S1a). Between May and August, SDD was on average lowest in Small Khanka, higher in China's Khanka, and highest in Russia's section of Khanka Lake. While in September-October, SDD was roughly

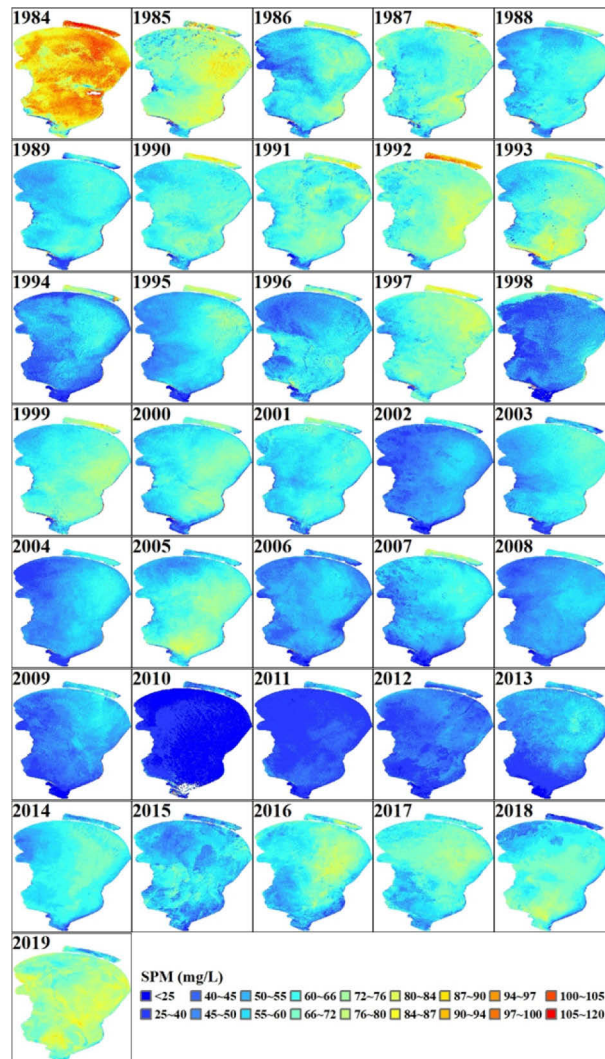


Fig. 6. Spatial distribution of mean annual (1984–2019) concentration of suspended particulate matter (SPM) across Lake Khanka derived from Landsat images.

equivalent in Small Khanka and in the Russia's section of Khanka Lake, and slightly higher in the China's section of Khanka.

The monthly variation in SPM showed the opposite of the trend observed with SDD. The average SPM concentration of Lake Khanka was lowest in May (50.16 ± 23.03 mg/L) and highest in October (70.29 ± 16.62 mg/L) (Fig. 7(b)). In May, SPM concentration was highest in China's Khanka, and the lowest in Small Khanka and Russia's Khanka. From June on, SPM concentration in Small Khanka was consistently the highest. In July-August, SPM concentration was still higher in the China's than in the Russia's section of Khanka Lake, while after September SPM concentration was similar in both the China's and Russia's section of Khanka Lake.

A year-to-year examination of the monthly variation of SDD and SPM during the 2000–2019 period is presented in Figure S2. Overall, monthly mean SDD and SPM was relatively stable in October, while large fluctuations were observed during the month of May. The amplitude of

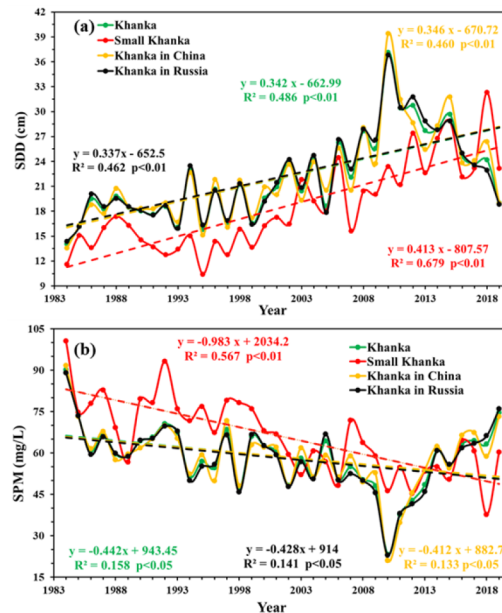


Fig. 7. Temporal trend (1984–2019) in secchi disk depth (SDD) (a), and suspended particulate matter (SPM) (b) over the entire lake and in different lacustrine regions of Lake Khanka. The dash lines represent the best-fit lines obtained by linear regression.

these fluctuations was much greater for SPM than for SDD, suggesting that SPM could be a more sensitive indicator than SDD of Lake Khanka's response to environmental changes.

4. Discussion

4.1. Comparison and evaluation of typical retrieval algorithms

Many algorithms have been developed to obtain remote estimates of SDD using satellite images. However, compared to some models with complex parameter requirements and higher atmospheric correction accuracy, empirical algorithms are relatively easy to derive and use [49]. Furthermore, several studies have also demonstrated the good performance of empirical models [10,12,50]. To select the best SDD empirical model to apply to Lake Khanka, several models were evaluated based on how well SDD measured in-situ compares with estimates of SDD derived from Landsat and MODIS images (Table S3; only models with $R^2 > 0.1$ are listed). In addition to R^2 , RMSE and MRE were also considered in these evaluations. Finally, the green/red band ratio model, adjusted from [20], was found suitable for SDD estimation in Lake Khanka, using both Landsat and MODIS images.

A major challenge to determination of lacustrine SDD and SPM from satellite imagery stems from the inherent optical properties of different materials comprising the pool of SPM in natural waters. Depending on the hydro-geomorphological settings, the size, density, composition and optical properties of particulate matter in lacustrine environments can vary greatly, making it therefore challenging to develop a universal retrieval algorithm for SPM [46,48]. In the present study, in order to select the SPM algorithm most suitable for Lake Khanka, several models were tested (Table S4). Results showed that most of the algorithms performed unsatisfactorily ($R^2 < 0.6$, and higher MRE than 20% and RMSE). Therefore, a novel SPMI algorithm was established to derive SPM concentration across Lake Khanka from Landsat and MODIS images.

4.2. Transferability of SPMI algorithms

Although SPMI has been successfully applied to Lake Khanka, its applicability to other lakes needs to be testified. In order to examine the transferability and robustness of SPMI, three large shallow lakes similar to Lake Khanka were selected. They include Lake Hulun, Hongze and Chao, their location and sampling sites of SPM were demonstrated in Fig. 8. Matching point-pairs between in-situ measured SPM and spectral information from processed images (MOD09GA/MYD09GA) collected within 48 hours of these measurements were used to develop SPM retrieval models. After deleting invalid points caused by land-water boundary, cloud/shadow-contaminated pixels, a total of 90 matched pairs were reserved for MODIS images. Random 2/3 of the synchronous dataset ($N = 60$) were selected to construct the model, and the remaining 1/3 of the samples ($N = 30$) were used for model validation. The calibration and validation dataset confirmed that the SPMI-based model can yield satisfactory results (Figure S3).

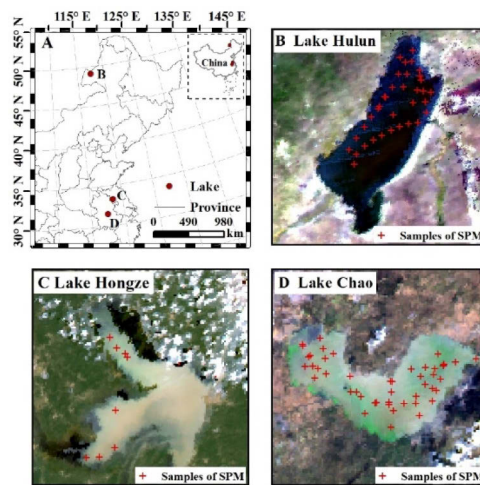


Fig. 8. Location of lakes Hulun, Hongze, Chao in China, and distribution of sampling sites where suspended particulate matter (SPM) was measured.

From Figure S3, the algorithms based on SPMI produced reasonably accurate results as shown by the high determination coefficients ($R^2 = 0.77$, $p < 0.001$). In the calibration dataset, almost all the data points fell within the 95% confidence interval. Furthermore, the MRE and RMSE values were only 25.86%, 11.85 mg/L, respectively. Measured and estimated SPM values were evenly distributed along the 1:1 line. Based on past literatures and our researches [16,51], the optical properties of the above four lakes are different, but they are all shallow lakes. Hence, we could infer that SPMI is a promisingly transferable and robust algorithm for SPM determination in shallow lakes.

4.3. Applicability of SDD and SPM models to Lake Khanka in Russia

Lake Khanka located on the border between China and Russia, making it a challenge to access the entire lake for the study. Unlike with other studies in-situ measurements were made throughout entire lakes [9,52–53], in the present investigation our measurements were limited to the China's section of Lake Khanka. No data from published literature was found regarding the Russia's section of Lake Khanka. An important question to resolve in this study was how to verify the reliability of the estimates derived for the Khanka in Russia. As described in sections 2.4 and 2.5, the SDD and SPM retrieval models based on Landsat and MODIS images are relatively independent. Therefore, reliability of the results can be assessed through correlation

and consistency between remote estimates obtained using Landsat and MODIS images collected in the same day. Since the Landsat images used in this study were collected using three sensors (TM, ETM+ and OLI) over the period of observation, three separate calibration and verification were necessary to account for differences among sensors in terms of signal-to-noise ratio, band bandwidth, and sensitivity. Results of these calibration and validation exercises for retrieval of SDD and SPM are reported in Figure S4.

Retrieval results from MODIS and OLI were evenly distributed along the 1:1 line (Figure S4a and S4d), with an MRE of 5.17% SDD and 6.56% for SPM. The RMSE of SDD and SPM was 1.42 cm and 5.31 mg/L, respectively. Due to the different band composition involved in the SDD and SPM algorithms, there was difference in the calibration coefficient. For the SDD model, good consistency was found with ETM+ and OLI sensors, but the model needed to be adjusted a coefficient of 3/4 when applied to TM images (Initial SDD inversion results multiply 3/4). For the SPM model, the coefficient of adjustment was 3/5 when applied to both TM and ETM+ images (Initial SPM inversion results multiply 3/5).

For this long-term (36 years) examination of trend in SDD and SPM in Lake Khanka, Landsat images were selected primarily due to the longtime-span (1984–2019) of Landsat data acquisition. However, the revisit cycle of Landsat images was 8 days as opposed to only 0.5 day for MODIS satellites which have only been in operation since 2000. So, by combining data from these two satellites, the present study sought to maximize the benefits of Landsat and MODIS (Figure S5). Although in most years, the mean annual SDD and SPM based on MODIS images were slightly higher than those derived from Landsat images, the inter-annual trends were consistent. Indeed, for mean annual SDD and SPM concentration, the correlation coefficient between MODIS and Landsat was as high as 0.9 and 0.82, respectively. These results demonstrated the consistency of the results obtained by Landsat and MODIS sensors, thus confirming the internal validity of our research approach.

4.4. Mechanism of SDD response to climate change

4.4.1. Correlation among related climate and water parameters

Numerous studies have demonstrated that SDD variation in lacustrine systems is generally linked to SPM, Chla and DOC concentration [3,7,11]. However, the proportion of optically-active substances associated with these constituents varies from one lake to another [51,54]. Therefore, the dominant factors affecting SDD in different lakes are also very different. In order to determine the dominant factor influencing SDD variation in Lake Khanka, Pearson correlation and linear regression were conducted between in-situ Ln(SDD) and Ln(SPM), Ln(Chla) and Ln(DOC). Pearson correlation and R^2 between Ln(SDD) and Ln(SPM) were much higher than Ln(SDD) vs Ln(Chla), and Ln(SDD) vs Ln(DOC) (Figure S6). Although Chla and DOC may have had some influence on SDD, their effect appears to have been minimal compared to SPM. This assertion clearly warrants further investigation to determine its validity.

In order to disentangle the underlying mechanism of climate change on SDD, a single factor correlation was conducted among relevant factors. From the inter-annual curves of SPM and SDD variation in Lake Khanka, opposite trends between these two variables were observed (Fig. 7, Figure S5, and Figure S7a). SH is a significant parameter representing radiation increasing or decreasing, and noticeable variation was observed in recent decades [12,55]. Such variations could have direct effect on SDD variation in lacustrine ecosystems. Indeed, SH and SDD were significant positive correlated (Figure S7b). WDSP and PRCP have also been recognized as determining factors of SPM concentration in lakes [56–59]. However, because the effect of WDSP and PRCP on SDD is indirect and modulated through SPM, only the correlations between SPM and these variables (WDSP and PRCP) were analyzed (Figure S7c and S7e). Results showed positive effects of WDSP and PRCP on SPM in Lake Khanka. Therefore, the inter-annual

trend in SPM in Lake Khanka was resulted from variation in WDSP and PRCP. The relationship between TEMP and WDSP was also found to be negative (Figure S7f).

4.4.2. Response of SDD to climate change

From the above analysis and discussion, climate change may have played a role in the temporal trend of SDD in Lake Khanka. Although the trend lines between AP and SPM suggested negative correlations between these variables, these relationships were not significant (Figure S7d), therefore suggesting a limited contribution of these factors to the observed trend in SDD. Based on the other climatic factors, the following underlying mechanism is proposed and is illustrated in Fig. 9.

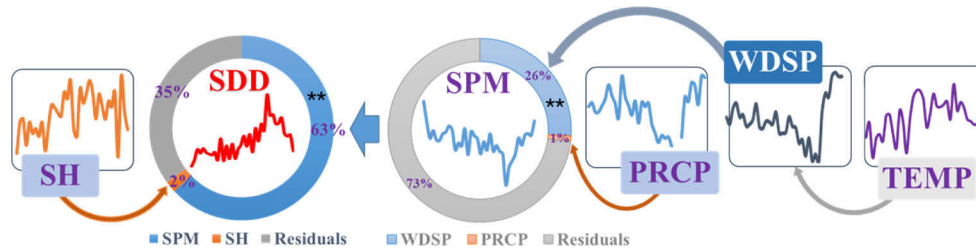


Fig. 9. The process of climate change on SDD variation in Lake Khanka. Significance levels are indicated as “***”, $p < 0.01$.

A close inspection of the results presented in Fig. 7 suggests two periods (1984~2009 and 2010~2019) for any climate-driven SDD variability in Lake Khanka with 2010 being an important turning point. Cold island effect is a type of microclimate effect created by large surface water bodies (wetlands, large lakes) characterized by higher specific heat capacity than the surrounding landscapes [60–63]. The strength of this cold island effect can be influenced by climate change [64,65]. It is possible that the significance of that effect during distinct time periods may have affected the inter-annual variability in SPM and SDD observed in Lake Khanka. More specifically, we speculated that during the first period (1984–2009), increase in land surface TEMP around Lake Khanka may have reduced the TEMP difference between the lake and surrounding terrestrial landscapes, finally resulted in decreased WDSP (Figure S8b, c). Because of the reduced WDSP, lake surface is less disturbed, and that would translate into limited sediment resuspension, combined with runoff reduction resulted from reduced precipitation (Figure S8d) [66,67], which above factors eventually lead low SPM concentration. In the second period (2010–2019), these mechanisms would operate in opposite direction compared to the first period. Along with a decrease in TEMP, the TEMP difference between surrounding landscapes and lake water would increase, and consequently WDSP increased (Figure S8b, c). Combined with increasing PRCP, that would ultimately lead to the increase in SPM observed between 2010~2019.

To clarify the contribution of $\text{Ln}(\text{SPM})$ and $\text{Ln}(\text{SH})$ to change in $\text{Ln}(\text{SDD})$ in the past 36 years, GLM regression was used. Results showed that the contribution of SPM and SH to the temporal variation in SDD was 63% and 2%, respectively. It is worth noting that in addition to their own correlation between SPM and SDD, the possible reason for SPM’s contribution to SDD change reaching 63% includes that SDD and SPM are both deduced from same images.

Furthermore, the contribution of $\text{Ln}(\text{WDSP})$ and $\text{Ln}(\text{PRCP})$ to change in $\text{Ln}(\text{SPM})$ was 26% and 1%, respectively. Above results further demonstrated that the influence of WDSP on SPM is much greater than that of PRCP.

5. Conclusions

The spatiotemporal (1984 to 2019) variations of SDD and SPM in Lake Khanka were examined. For that analysis, a novel index SPMI was developed, through incorporation of SPM concentration effect on spectral radiance, and satisfactorily applied to Landsat ($R^2 = 0.70$, $p < 0.001$) and MODIS ($R^2 = 0.78$, $p < 0.001$) images to obtain remote estimates of SPM concentration. For SDD, a significant increasing trend was observed over the past 36 years, with a maximum around 2010 and then a slowly descending trend thereafter. Contrary to the trend in SDD, SPM showed a continuously decreasing trend over that 36-year period, but a slowly increasing trend since 2010. In support of our original hypothesis, results showed that SPM dominated the temporal variation in SDD and explained 63% of the variability in the data (compared to only 2% due to SH). Based on these results, we further proposed that variation in wind speed, driven by the so-called “cold island effect” may have been the primary driver of SPM and SDD variation in Lake Khanka. That effect was probably stronger between 1984–2009, due to greater difference in temperature between lake surface and surrounding landscapes than after 2010 (equal warming of both land and water). An illustration of the mechanism linking TEMP gradient and WDSP is presented to explain how temperature-induced disturbance may have caused sediment resuspension, ultimately controlling lake clarity (as expressed by SDD) in Lake Khanka. This analysis furthers our understanding of the interconnections between climatic factors and water quality in large shallow lakes.

Funding. National Natural Science Foundation of China (42101366, 51925902, 41730104, 42071336, 42171385, 42001311)

Acknowledgments. This research was financially supported by the Natural Science Foundation of China (42101366, 51925902, 41730104, 42071336, 42171385, 42001311). Acknowledgement for the data support from “National Geographic Resource Science SubCenter, National Earth System Science Data Center, National Science & Technology Infrastructure of China. (<http://gre.geodata.cn>)”. The authors gratefully acknowledge the contribution of three anonymous reviewers and the editorial staff for their constructive comments on an early version of this paper.

Disclosures. The authors declare no conflicts of interest.

Data availability. Data underlying the results presented in this paper are not publicly available at this time but may be obtained from the authors upon reasonable request.

Supplemental document. See [Supplement 1](#) for supporting content.

References

1. J. Wang, Y. Sheng, and T. S. D. Tong, “Monitoring decadal lake dynamics across the Yangtze Basin downstream of Three Gorges Dam,” *Remote Sens. Environ.* **152**, 251–269 (2014).
2. X. H. Pi, L. Feng, W. F. Li, D. Zhao, X. X. Kuang, and J. S. Li, “Water clarity changes in 64 large alpine lakes on the Tibetan Plateau and the potential responses to lake expansion,” *ISPRS J. Photogramm. Remote Sens.* **170**, 192–204 (2020).
3. D. Liu, H. T. Duan, S. Loisel, C. M. Hu, G. Q. Zhang, J. L. Li, H. Yang, J. R. Thompson, Z. G. Cao, M. Shen, R. H. Ma, M. Zhang, and W. X. Han, “Observations of water transparency in China’s lakes from space,” *International Journal of Applied Earth Observation and Geoinformation* **92** (2020).
4. M. Shen, H. T. Duan, Z. G. Cao, K. Xue, T. C. Qi, J. G. Ma, D. Liu, K. S. Song, C. L. Huang, and X. Y. Song, “Sentinel-3 OLCI observations of water clarity in large lakes in eastern China: Implications for SDG 6.3.2 evaluation,” *Remote Sens. Environ.* **247**, 111950 (2020).
5. P. Y. Baklanov, A. N. Kachur, V. V. Ermoshin, S. I. Kozhenkova, A. N. Makhinov, A. N. Bugaets, V. B. Bazarova, V. I. Kim, and V. V. Shamov, “Current Geo-Ecological Problems Within the Lake Khanka Drainage Basin,” *Geogr. Nat. Resour.* **40**(4), 325–334 (2019).
6. Z. P. Lee, S. L. Shang, K. P. Du, and J. W. Wei, “Resolving the long-standing puzzles about the observed Secchi depth relationships,” *Limnol. Oceanogr.* **63**(6), 2321–2336 (2018).
7. S. L. Wang, J. S. Li, B. Zhang, Z. Lee, E. Spyros, L. Feng, C. Liu, H. L. Zhao, Y. H. Wu, L. P. Zhu, L. M. Jia, W. Wan, F. F. Zhang, Q. Shen, A. N. Tyler, and X. F. Zhang, “Changes of water clarity in large lakes and reservoirs across China observed from long-term MODIS,” *Remote Sens. Environ.* **247**, 111949 (2020).
8. I. M. McCullough, C. S. Loftin, and S. A. Sader, “Combining lake and watershed characteristics with Landsat TM data for remote estimation of regional lake clarity,” *Remote Sens. Environ.* **123**, 109–115 (2012).

9. K. Shi, Y. L. Zhang, G. W. Zhu, B. Q. Qin, and D. L. Pan, "Deteriorating water clarity in shallow waters: Evidence from long term MODIS and in-situ observations," *International Journal of Applied Earth Observation and Geoinformation* **68**, 287–297 (2018).
10. K. S. Song, G. Liu, Q. Wang, Z. D. Wen, L. L. Lyu, Y. X. Du, L. W. Sha, and C. Fang, "Quantification of lake clarity in China using Landsat OLI imagery data," *Remote Sens. Environ.* **243**, 111800 (2020).
11. L. Feng, X. J. Hou, and Y. Zheng, "Monitoring and understanding the water transparency changes of fifty large lakes on the Yangtze Plain based on long-term MODIS observations," *Remote Sens. Environ.* **221**, 675–686 (2019).
12. Y. L. Zhang, B. Q. Qin, K. Shi, Y. B. Zhang, J. M. Deng, M. Wild, L. Li, Y. Q. Zhou, X. L. Yao, M. Liu, G. W. Zhu, L. Zhang, B. H. Gu, and J. D. Brookes, "Radiation dimming and decreasing water clarity fuel underwater darkening in lakes," *Sci. Bull.* **65**(19), 1675–1684 (2020).
13. R. E. Carlson, "A trophic state index for lakes 1," *Limnol. Oceanogr.* **22**(2), 361–369 (1977).
14. P. D. Biber, H. W. Paerl, C. L. Gallegos, and W. J. Kenworthy, "Evaluating indicators of seagrass stress to light," *Estuarine indicators*, 193–209 (2005).
15. L. G. Olmanson, P. L. Brezonik, J. C. Finlay, and M. E. Bauer, "Comparison of Landsat 8 and Landsat 7 for regional measurements of CDOM and water clarity in lakes," *Remote Sens. Environ.* **185**, 119–128 (2016).
16. C. Fang, K. Song, Y. Shang, J. Ma, Z. Wen, and J. Du, "Remote sensing of harmful algal blooms variability for Lake Hulun using adjusted FAI (AFAI) algorithm," *J. Environ. Inf.* (2018), <https://www.doi.org/10.3808/jei.201700385>.
17. L. G. Olmanson, M. E. Bauer, and P. L. Brezonik, "A 20-year Landsat water clarity census of Minnesota's 10,000 lakes," *Remote Sens. Environ.* **112**(11), 4086–4097 (2008).
18. N. Sriwongsitanon, K. Surakit, and S. Thianpopirug, "Influence of atmospheric correction and number of sampling points on the accuracy of water clarity assessment using remote sensing application," *J. Hydrol.* **401**(3-4), 203–220 (2011).
19. B. P. Page, L. G. Olmanson, and D. R. Mishra, "A harmonized image processing workflow using Sentinel-2/MSI and Landsat-8/OLI for mapping water clarity in optically variable lake systems," *Remote Sens. Environ.* **231**, 111284 (2019).
20. H. Duan, R. Ma, Y. Zhang, and B. Zhang, "Remote-sensing assessment of regional inland lake water clarity in northeast China," *Limnology* **10**(2), 135–141 (2009).
21. F. L. Lobo, M. P. Costa, and E. M. Novo, "Time-series analysis of Landsat-MSS/TM/OLI images over Amazonian waters impacted by gold mining activities," *Remote Sens. Environ.* **157**, 170–184 (2015).
22. Z. Lee, S. Shang, L. Qi, J. Yan, and G. Lin, "A semi-analytical scheme to estimate Secchi-disk depth from Landsat-8 measurements," *Remote sensing of environment* **177**, 101–106 (2016).
23. Z. Lee, S. Shang, C. Hu, K. Du, A. Weidemann, W. Hou, J. Lin, and G. Lin, "Secchi disk depth: A new theory and mechanistic model for underwater visibility," *Remote sensing of environment* **169**, 139–149 (2015).
24. T. Rodrigues, E. Alcantara, F. Watanabe, and N. Imai, "Retrieval of Secchi disk depth from a reservoir using a semi-analytical scheme," *Remote Sens. Environ.* **198**, 213–228 (2017).
25. K. C. Rose, S. R. Greb, M. Diebel, and M. G. Turner, "Annual precipitation regulates spatial and temporal drivers of lake water clarity," *Ecol Appl* **27**(2), 632–643 (2017).
26. Z. Cao, H. Duan, L. Feng, R. Ma, and K. Xue, "Climate- and human-induced changes in suspended particulate matter over Lake Hongze on short and long timescales," *Remote Sens. Environ.* **192**, 98–113 (2017).
27. C. Y. Fan, C. Q. Song, K. Liu, L. H. Ke, B. Xue, T. Chen, C. S. Fu, and J. Cheng, "Century-Scale Reconstruction of Water Storage Changes of the Largest Lake in the Inner Mongolia Plateau Using a Machine Learning Approach," *Water Resources Research* **57** (2021).
28. H. T. Duan, Z. G. Cao, M. Shen, D. Liu, and Q. T. Xiao, "Detection of illicit sand mining and the associated environmental effects in China's fourth largest freshwater lake using daytime and nighttime satellite images," *Sci. Total Environ.* **647**, 606–618 (2019).
29. W. Zou, K. T. Tolonen, G. W. Zhu, B. Q. Qin, Y. L. Zhang, Z. G. Cao, K. Peng, Y. J. Cai, and Z. J. Gong, "Catastrophic effects of sand mining on macroinvertebrates in a large shallow lake with implications for management," *Sci. Total Environ.* **695**, 133706 (2019).
30. K. Song, C. Fang, P.-A. Jacinthe, Z. Wen, G. Liu, X. Xu, Y. Shang, and L. Lyu, "Climatic versus Anthropogenic Controls of Decadal Trends (1983–2017) in Algal Blooms in Lakes and Reservoirs across China," *Environ. Sci. Technol.* **55**(5), 2929–2938 (2021).
31. B. Q. Qin, H. W. Paerl, J. D. Brookes, J. G. Liu, E. Jeppesen, G. W. Zhu, Y. L. Zhang, H. Xu, K. Shi, and J. M. Deng, "Why Lake Taihu continues to be plagued with cyanobacterial blooms through 10 years (2007–2017) efforts," *Sci. Bull.* **64**(6), 354–356 (2019).
32. L. A. Shchur, A. D. Aponasenko, V. P. Ladygina, V. N. Lopatin, and G. V. Makarskaya, "Investigation of bacterioplankton in the loess-containing Lake Khanka," *Microbiology* **69**(4), 466–470 (2000).
33. Z. D. Wen, K. S. Song, G. Liu, Y. X. Shang, J. B. Hou, L. L. Lyu, and C. Fang, "Impact factors of dissolved organic carbon and the transport in a river-lake continuum in the Tibet Plateau of China," *Journal of Hydrology* **579** (2019).
34. Z. D. Wen, K. S. Song, L. L. Lyu, C. Fang, Y. X. Shang, G. Liu, and J. Du, "A national-scale data set for dissolved carbon and its spatial pattern in lakes and reservoirs across China," *Sci. Data* **7**(1), 82 (2020).
35. K. S. Song, Z. D. Wen, Y. X. Shang, H. Yang, L. L. Lyu, G. Liu, C. Fang, J. Du, and Y. Zhao, "Quantification of dissolved organic carbon (DOC) storage in lakes and reservoirs of mainland China," *J. Environ. Manage.* **217**, 391–402 (2018).

36. K. S. Song, Z. D. Wen, P. A. Jacinthe, Y. Zhao, and J. Du, "Dissolved carbon and CDOM in lake ice and underlying waters along a salinity gradient in shallow lakes of Northeast China," *J. Hydrol.* **571**, 545–558 (2019).
37. G. Schmidt, C. B. Jenkinson, J. Masek, E. Vermote, and F. Gao, "*Landsat ecosystem disturbance adaptive processing system (LEDAPS) algorithm description*," (US Geological Survey, 2013).
38. U. Landsat, Surface Reflectance Code (LASRC) Product Guide.
39. E. Vermote, C. Justice, M. Claverie, and B. Franch, "Preliminary analysis of the performance of the Landsat 8/OLI land surface reflectance product," *Remote Sens. Environ.* **185**, 46–56 (2016).
40. Z. Zhu, S. X. Wang, and C. E. Woodcock, "Improvement and expansion of the Fmask algorithm: cloud, cloud shadow, and snow detection for Landsats 4-7, 8, and Sentinel 2 images," *Remote Sens. Environ.* **159**, 269–277 (2015).
41. P. Scaramuzza, E. Micijevic, and G. Chander, "SLC gap-filled products phase one methodology," *Landsat Technical Notes* **5** (2004).
42. C. Fang, K. Song, L. Li, Z. Wen, G. Liu, J. Du, Y. Shang, and Y. Zhao, "Spatial variability and temporal dynamics of HABs in Northeast China," *Ecological Indicators* **90**, 280–294 (2018).
43. H. Xu, "Modification of normalised difference water index (NDWI) to enhance open water features in remotely sensed imagery," *International journal of remote sensing* **27**(14), 3025–3033 (2006).
44. S. Tao, J. Fang, X. Zhao, S. Zhao, H. Shen, H. Hu, Z. Tang, Z. Wang, and Q. Guo, "Rapid loss of lakes on the Mongolian Plateau," *Proc Natl Acad Sci U S A* **112**(7), 2281–2286 (2015).
45. L. Feng, C. M. Hu, X. L. Chen, L. Q. Tian, and L. Q. Chen, "Human induced turbidity changes in Poyang Lake between 2000 and 2010: Observations from MODIS," *Journal of Geophysical Research-Oceans* **117** (2012).
46. S. V. Balasubramanian, N. Pahlevan, B. Smith, C. Binding, J. Schalles, H. Loisel, D. Gurlin, S. Greb, K. Alikas, M. Randla, M. Bunkai, W. Moses, N. Ha, M. K. Lehmann, D. O'Donnell, M. Ondrusek, T. H. Han, C. G. Fichot, T. Moore, and E. Boss, "Robust algorithm for estimating total suspended solids (TSS) in inland and nearshore coastal waters," *Remote Sens. Environ.* **246**, 111768 (2020).
47. L. Feng, C. Hu, X. Chen, and Q. Song, "Influence of the Three Gorges Dam on total suspended matters in the Yangtze Estuary and its adjacent coastal waters: Observations from MODIS," *Remote Sens. Environ.* **140**, 779–788 (2014).
48. X. Hou, L. Feng, H. Duan, X. Chen, D. Sun, and K. Shi, "Fifteen-year monitoring of the turbidity dynamics in large lakes and reservoirs in the middle and lower basin of the Yangtze River, China," *Remote Sens. Environ.* **190**, 107–121 (2017).
49. M. W. Matthews, "A current review of empirical procedures of remote sensing in inland and near-coastal transitional waters," *International Journal of Remote Sensing* **32**(21), 6855–6899 (2011).
50. J. L. Ren, Z. B. Zheng, Y. M. Li, G. N. Lv, Q. Wang, H. Lyu, C. C. Huang, G. Liu, C. G. Du, M. Mu, S. H. Lei, and S. Bi, "Remote observation of water clarity patterns in Three Gorges Reservoir and Dongting Lake of China and their probable linkage to the Three Gorges Dam based on Landsat 8 imagery," *Sci. Total Environ.* **625**, 1554–1566 (2018).
51. K. Xue, R. Ma, H. Duan, M. Shen, E. Boss, and Z. Cao, "Inversion of inherent optical properties in optically complex waters using sentinel-3A/OLCI images: A case study using China's three largest freshwater lakes," *Remote Sens. Environ.* **225**, 328–346 (2019).
52. D. L. Jiang, B. Matsushita, F. Setiawan, and A. Vundo, "An improved algorithm for estimating the Secchi disk depth from remote sensing data based on the new underwater visibility theory," *ISPRS J. Photogramm. Remote Sens.* **152**, 13–23 (2019).
53. X. Xu, X. L. Huang, Y. L. Zhang, and D. Yu, "Long-Term Changes in Water Clarity in Lake Liangzi Determined by Remote Sensing," *Remote Sens.* **10**(9), 1441 (2018).
54. G. Liu, L. Li, K. Song, Y. Li, H. Lyu, Z. Wen, C. Fang, S. Bi, X. Sun, and Z. Wang, "An OLCI-based algorithm for semi-empirically partitioning absorption coefficient and estimating chlorophyll a concentration in various turbid case-2 waters," *Remote Sens. Environ.* **239**, 111648 (2020).
55. M. Wild, H. Gilgen, A. Roesch, A. Ohmura, C. N. Long, E. G. Dutton, B. Forgan, A. Kallis, V. Russak, and A. Tsvetkov, "From dimming to brightening: Decadal changes in solar radiation at Earth's surface," *Science* **308**(5723), 847–850 (2005).
56. K. Xue, R. H. Ma, M. Shen, Y. Li, H. T. Duan, Z. G. Cao, D. Wang, and J. F. Xiong, "Variations of suspended particulate concentration and composition in Chinese lakes observed from Sentinel-3A OLCI images," *Sci. Total Environ.* **721**, 137774 (2020).
57. S. H. Lei, J. Xu, Y. M. Li, C. G. Du, G. Liu, Z. B. Zheng, Y. F. Xu, H. Lyu, M. Mu, S. Miao, S. Zeng, J. F. Xu, and L. L. Li, "An approach for retrieval of horizontal and vertical distribution of total suspended matter concentration from GOCI data over Lake Hongze," *Sci. Total Environ.* **700**, 134524 (2020).
58. S. Kratzer, D. Kyriliuk, and C. Brockmann, "Inorganic suspended matter as an indicator of terrestrial influence in Baltic Sea coastal areas - Algorithm development and validation, and ecological relevance," *Remote Sens. Environ.* **237**, 111609 (2020).
59. D. Liu, Y. Bai, X. Q. He, B. Y. Tao, D. L. Pan, C. T. A. Chen, L. Zhang, Y. Xu, and C. H. Gong, "Satellite estimation of particulate organic carbon flux from Changjiang River to the estuary," *Remote Sens. Environ.* **223**, 307–319 (2019).
60. R. Sun, A. Chen, L. Chen, and Y. Lu, "Cooling effects of wetlands in an urban region: The case of Beijing," *Ecological Indicators* **20**, 57–64 (2012).
61. H. Saaroni and B. Ziv, "The impact of a small lake on heat stress in a Mediterranean urban park: the case of Tel Aviv, Israel," *Int J Biometeorol* **47**(3), 156–165 (2003).

62. Y. Huang, H. X. Liu, K. Hinkel, B. L. Yu, R. Beck, and J. P. Wu, "Analysis of Thermal Structure of Arctic Lakes at Local and Regional Scales Using in Situ and Multidate Landsat-8 Data," *Water Resources Research* **53**(11), 9642–9658 (2017).
63. S. Haddout, H. Qanza, M. A. Guennoun, H. Azidane, R. Karra, and A. Essaidi, "Epilimnion and metalimnion thermal water temperature variables in Moroccan's Lakes using a one-dimensional fresh-water lake model," *International Journal of River Basin Management* **18**(3), 321–333 (2020).
64. Y. Wu, A. N. Huang, B. Yang, G. T. Dong, L. J. Wen, Z. Q. Lazhu, Z. P. Zhang, X. Y. Fu, X. D. Zhu, S. X. Zhang, and Cai, "Numerical study on the climatic effect of the lake clusters over Tibetan Plateau in summer," *Clim Dyn* **53**(9-10), 5215–5236 (2019).
65. E. Roget and V. M. Khan, "Decadal differences of the diurnal temperature range in the Aral Sea region at the turn of the century," *Tellus A: Dynamic Meteorology and Oceanography* **70**(1), 1–12 (2018).
66. V. Lakshmi, J. Fayne, and J. Bolten, "A comparative study of available water in the major river basins of the world," *J. Hydrol.* **567**, 510–532 (2018).
67. J. Hu, J. Ma, C. Nie, L. Xue, Y. Zhang, F. Ni, Y. Deng, J. Liu, D. Zhou, L. Li, and Z. Wang, "Attribution Analysis of Runoff Change in Min-Tuo River Basin based on SWAT model simulations, China," *Scientific Reports* **10** (2020).